Hindawi
Mathematical Problems in Engineering
Volume 2020, Article ID 2859310, 10 pages
https://doi.org/10.1155/2020/2859310

Research Article

Dynamic Modeling of Gear System Based on 3D Finite Element Model and Its Application in Spalling Fault Analysis

Zhiguo Wan, Yihua Dou, Yuan Guan, Qi Meng, and Suobin Li

School of Mechanical Engineering, Xi'an Shiyou University, Xi'an 710065, China

Correspondence should be addressed to Zhiguo Wan; zgwan@xsyu.edu.cn

Received 8 August 2019; Revised 20 December 2019; Accepted 3 February 2020; Published 19 March 2020

Academic Editor: Pablo Lopez-Crespo

A reduced-order dynamic model, based on three-dimensional (3D) finite element model (FEM) and component modal synthesis technique (CMS), was presented for simulating the dynamic behavior of the spur gear system. The gear shaft and gear body were established via 3D elements to simulate bending and torsion of the gear system. The CMS technique was used to generate a reduced-order model of a spur gear system. A pair of mating teeth was assimilated to two different foundations (one for the pinion tooth and the other one for the gear tooth) linked in series by some independent springs, which was used to simulate the contact stiffness. The validity of the proposed model was verified by static analysis, dynamic analysis, and experimental analysis. The results show that the proposed model is an effective model. In addition, the proposed model has also been applied to analyze spur gear spalling faults. The results show that the dynamic response of the gear system is periodic vibration shock response due to the alternate meshing of single and double teeth. When the spalling fault occurs, some shock responses with significantly enhanced amplitude will be generated as the result of contact loss.

1. Introduction

Structural dynamical monitoring and fault diagnosis are of great importance to diagnose faults/failures of structures [1]. In order to facilitate the development of diagnostic and prognostic techniques for gear faults, many researchers worked on the gear dynamic modeling to ascertain the effect of gear defects on the vibration response. The first class of modeling method is the lumped parameter model. Ma et al. used a four degrees of freedom (DOF) gear dynamic model to study the dynamic and vibration characteristics of the gear system with local defects [2]. Chen et al. used a 6-DOF gear dynamic model to study the vibration of spur gear with tooth root crack propagating along tooth width and crack depth [3]. Kang et al. investigated the dynamic behaviors of the gear-rotor system with viscoelastic supports under residual shaft bow effect [4]. Bartelmus et al. dealt with mathematical modeling and computer simulation as a tool for aiding gearboxes diagnostic inference [5]. Xiong et al. used single DOF model to investigate the effect of backlash on the nonlinear dynamic characteristics [6]. Wang et al. established a 3-DOF torsional vibration model and investigated the effects of the pinion speed and stiffness on the dynamic behavior of the gear transmission system [7]. Yang et al. investigated the effects of tooth breakage size and rotational speed on the vibration response of the planetary gearbox [8]. A simplified nonlinear lumped parameter model with 6-DOF established by Mohamed was developed to simulate the vibration response of faulty external spur gears [9]. Chen et al. developed a lumped parameter model to study the dynamic response of the gear system with different crack sizes [10]. The second approach is the hybrid beam element/lumped models. In this model, the beam elements are used to model the shafts and a pair of rigid disks is connected by a spring damper with time-varying mesh stiffness for modeling a pair of mating teeth. Wan et al. used this method to investigate the effect of tooth crack on the vibration response [11]. Han et al. analyzed the effects of position and type of the rotor crack (transverse or slant crack) on the gear system dynamic behaviors by this kind of dynamic model [12, 13]. Ma et al. analyzed the fault feature of cracked gear [14, 15]. Yu et al. used this model to study the dynamic coupling behavior of the transverse and

rotational motions of gears subjected to gear eccentricities [16]. The first two models are relatively mature and have been used to analyze typical faults such as crack faults [17, 18]. In addition, some researchers discussed the contact characteristic and gear geometry with existence of radial and angular eccentric errors [19]. Another model is the 3D finite element model. In recent years, the finite element modeling of some microstructure small cracks has made great progress [20–22]. However, it needs to be further studied in the equipment level system modeling, such as the gear system. Because the FEM is much computationally expensive compared with the first two models and mostly limited to quasi-static approaches [23, 24]. To address this problem, a reduced-order gear dynamic model based on 3D FEM and CMS technique is presented and used to solve fast solution problems of 3D FEM. In addition, this model has also been applied to analyze spur gear spalling faults.

This paper is organized as follows. In Section 2, the 3D FEM of a spur gear system was developed. The Craig–Bampton component modal synthesis technique was used to generate a reduced-order model of the gear system. In Section 3, the tooth contact was modeled by using the time-varying elastic foundations (Pasternak foundations). In Section 4, the driving and driven gears are connected by the elastic foundation and the dynamic equations of the gear system are deduced. In Section 5, the equations of motion were solved by Newmark-β integration and the vibration characteristic of a gear system with/without spalling fault were simulated and discussed. Conclusions are given in Section 6.

2. The Gear Dynamic Model Based on Craig–Bampton Component Modal Synthesis Technique

Figure 1 shows the process of establishing the 3D FEM models of a spur gear system. Firstly, the FEM of the driving and the driven shaft is obtained by software HYPERMESH and ANSYS. The reduced-order model can be generated by Craig–Bampton component modal synthesis technique. Then, the driving and the driven gear are connected by an elastic foundation with time-varying stiffness [23, 25]. Finally, the dynamic equations are derived and solved by Newmark-β integration. The details of every step mentioned above are addressed in the following sections.

2.1. The Reduced-Order Model of Driving or Driven Gear. A 3D FEM of driving shaft of a gear system is shown in Figure 2. There are more than 3,000 nodes and 9,000 degrees of freedom in this model. It will be very time-consuming to solve the model directly. Thus, a reduced-order model is demanded for dynamic analysis. Component mode synthesis technique is a kind of efficient model reduction method. The Craig–Bampton (CB) component mode synthesis method is utilized in this paper.

As shown in Figure 2, according to the structure characteristic of the gear system, the 3D FEM of the driving shaft (including pinion and shaft) is divided into two substructures. They are named as the shaft substructure and the gear substructure, respectively. The interface of the two substructures is the axle hole of the gear. The main applications of CMS on this model are briefly summarized as follows.

Assume that the physical coordinate of the driving shaft can be expressed as follows:

$$\mathbf{x}_p = \left[\mathbf{x}_i^s, \mathbf{x}_k^s, \mathbf{x}_j^s, \mathbf{x}_i^g, \mathbf{x}_k^g, \mathbf{x}_j^g\right]^T, \tag{1}$$

where the subscripts "i"and "j" represent the internal node DOF and interface node DOF, respectively. "p" means stand for pinion, "k" denotes the kept DOFs used to connect the elastic foundation used to simulate tooth contact, andn the superscripts "s" and "g" represent the shaft substructure and the gear substructure.

The mass and stiffness matrix of the shaft substructure was obtained by finite element analysis software and arranged in order:

$$\mathbf{M}_p^s = \begin{bmatrix} \mathbf{M}_{ii} & \mathbf{M}_{ik} & \mathbf{M}_{ij} \\ \mathbf{M}_{ki} & \mathbf{M}_{kk} & \mathbf{M}_{kj} \\ \mathbf{M}_{ji} & \mathbf{M}_{jk} & \mathbf{M}_{jj} \end{bmatrix},$$
$$\mathbf{K}_p^s = \begin{bmatrix} \mathbf{K}_{ii} & \mathbf{K}_{ik} & \mathbf{K}_{ij} \\ \mathbf{K}_{ki} & \mathbf{K}_{kk} & \mathbf{K}_{kj} \\ \mathbf{K}_{ji} & \mathbf{K}_{jk} & \mathbf{K}_{jj} \end{bmatrix}, \tag{2}$$

where $\mathbf{M}_{ii}$, $\mathbf{M}_{kk}$, and $\mathbf{M}_{jj}$ are the mass matrix corresponding to internal node, kept node, and interface node, and other mass matrices are coupling matrices between different nodes. The meaning of the subscript of the stiffness matrix is the same as that of the mass matrix.

By fixing all the interface coordinates, the branch characteristic equation of the fixed interface is obtained:

$$\left(\mathbf{K}_{ii} - \omega^2 \mathbf{M}_{ii}\right)\mathbf{\Phi}^s = 0, \tag{3}$$

where $\mathbf{\Phi}^s$ is normal modes and ω is Natural frequency.

Additional constraints are introduced into all the interface DOF of the substructure, and then these interface DOF generate unit displacement in turn. The constraint modes can be obtained by solving the static balance problem:

$$\begin{bmatrix} \mathbf{K}_{ii} & \mathbf{K}_{ik} & \mathbf{K}_{ij} \\ \mathbf{K}_{ki} & \mathbf{K}_{kk} & \mathbf{K}_{kj} \\ \mathbf{K}_{ji} & \mathbf{K}_{jk} & \mathbf{K}_{jj} \end{bmatrix} \begin{bmatrix} \mathbf{\psi}_{ik}^s & \mathbf{\psi}_{ij}^s \\ \mathbf{I}_{kk} & 0 \\ 0 & \mathbf{I}_{jj} \end{bmatrix} = \begin{bmatrix} 0 & 0 \\ \mathbf{R}_{kk} & \mathbf{R}_{kj} \\ \mathbf{R}_{jk} & \mathbf{R}_{jj} \end{bmatrix}, \tag{4}$$

where $\mathbf{R}_{kk}$, $\mathbf{R}_{kj}$, $\mathbf{R}_{jk}$, and $\mathbf{R}_{jj}$ are the reaction force when the unit displacement is applied on the interface. $\mathbf{\psi}_{ik}^s$ and $\mathbf{\psi}_{ij}^s$ are the residual constraint modes of the elastic foundation node and the fixed interface, respectively.

The constraint modal set of substructure can be obtained by solving the following formula:

$$\mathbf{\Psi}_{ik}^s = -\mathbf{K}_{ii}^{-1}\mathbf{K}_{ik},$$
$$\mathbf{\Psi}_{ij}^s = -\mathbf{K}_{ii}^{-1}\mathbf{K}_{ij}. \tag{5}$$

The DOFs' transformation equations between physical coordinates and modal coordinates of the shaft can be written as follows:

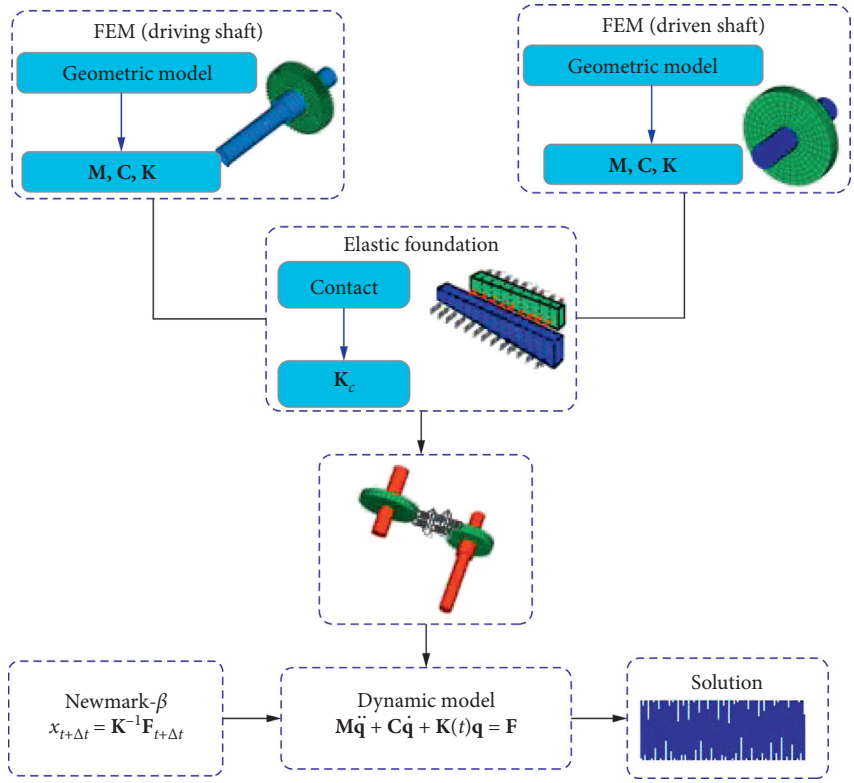

Figure 1: The establishment process of the dynamic model of a gear system.

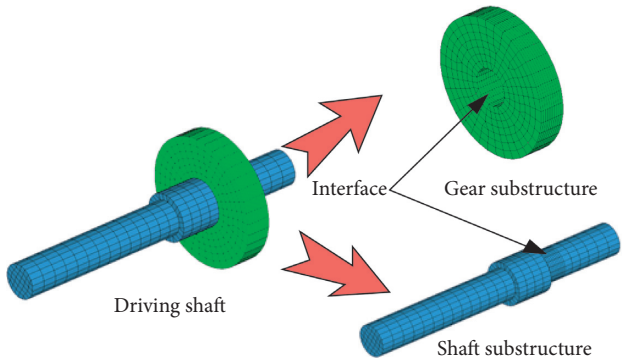

Figure 2: The 3D FEM of a driving shaft.

$$\mathbf{x}_p^s = \begin{Bmatrix} \mathbf{x}_i^s \\ \mathbf{x}_k^s \\ \mathbf{x}_j^s \end{Bmatrix} = \begin{bmatrix} \boldsymbol{\varphi}_{ir}^s & \boldsymbol{\psi}_{ik}^s & \boldsymbol{\psi}_{ij}^s \\ 0_{kr}^s & \mathbf{I}_{kk}^s & 0_{kj}^s \\ 0_{jr}^s & 0_{jk}^s & \mathbf{I}_{jj}^s \end{bmatrix}^s \begin{Bmatrix} \mathbf{p}_r^s \\ \mathbf{p}_k^s \\ \mathbf{p}_j^s \end{Bmatrix} = \boldsymbol{\varphi}_p^s \mathbf{P}_p^s, \tag{6}$$

where $\boldsymbol{\varphi}_{ir}^s$ denotes a truncated set of normal modes $\boldsymbol{\Phi}^s$ and $\mathbf{p}_r^s$, $\mathbf{p}_k^s$, and $\mathbf{p}_j^s$ are the model coordinates corresponding to the mode mentioned above.

Then, the mass matrix, stiffness matrix, and force vector of the shaft substructure in the model coordinate can be expressed as follows:

$$\begin{aligned} \mathbf{M}_{pm}^s &= \boldsymbol{\varphi}_p^{sT} \mathbf{M}_p^s \boldsymbol{\varphi}_p^s, \\ \mathbf{K}_{pm}^s &= \boldsymbol{\varphi}_p^{sT} \mathbf{K}_p^s \boldsymbol{\varphi}_p^s, \\ \mathbf{f}_{pm}^s &= \boldsymbol{\varphi}_p^{sT} \mathbf{f}_p^s, \end{aligned} \tag{7}$$

where $\mathbf{M}_p^s$, $\mathbf{K}_p^s$, and $\mathbf{f}_p^s$ denote the mass matrix, stiffness matrix, and force vector in the physical coordinate.

Similarly, the mass matrix $\mathbf{M}_{pm}^g$, stiffness matrix $\mathbf{K}_{pm}^g$, and force vector $\mathbf{f}_{pm}^g$ of the gear substructure in the model coordinate can be obtained by the same way.

The removed fix-interface coordinates are synthesized by using interface displacement compatibility conditions:

$$\mathbf{q}_p = \begin{Bmatrix} \mathbf{p}_r^s \\ \mathbf{p}_k^s \\ \mathbf{p}_j^s \\ \mathbf{p}_j^g \\ \mathbf{p}_k^g \\ \mathbf{p}_j^g \end{Bmatrix} = \begin{bmatrix} \mathbf{I} & 0 & 0 & 0 & 0 \\ 0 & \mathbf{I} & 0 & 0 & 0 \\ 0 & 0 & 0 & 0 & \mathbf{I} \\ 0 & 0 & \mathbf{I} & 0 & 0 \\ 0 & 0 & 0 & \mathbf{I} & 0 \\ 0 & 0 & 0 & 0 & \mathbf{I} \end{bmatrix} \begin{Bmatrix} \mathbf{p}_r^s \\ \mathbf{p}_k^s \\ \mathbf{p}_j^g \\ \mathbf{p}_k^g \\ \mathbf{p}_j \end{Bmatrix} = \mathbf{S}\mathbf{p}_p, \tag{8}$$

where $\mathbf{S}$ is the transfer matrix used to remove the non-independent coordinate.

The mass matrix, stiffness matrix, and force vector of the driving shaft in the independent model coordinate can be expressed as follows:

$$\begin{aligned} \mathbf{M}_p &= \mathbf{S}^T \mathbf{M}_{pm} \mathbf{S}, \\ \mathbf{K}_p &= \mathbf{S}^T \mathbf{K}_{pm} \mathbf{S}, \\ \mathbf{f}_p &= \mathbf{S}^T \mathbf{f}_{pm}, \end{aligned} \tag{9}$$

where $\mathbf{M}_{pm} = \begin{bmatrix} \mathbf{M}_{pm}^s & 0 \\ 0 & \mathbf{M}_{pm}^g \end{bmatrix}$, $\mathbf{K}_{pm} = \begin{bmatrix} \mathbf{K}_{pm}^s & 0 \\ 0 & \mathbf{K}_{pm}^g \end{bmatrix}$, and $\mathbf{f}_{pm} = \begin{Bmatrix} \mathbf{f}_{pm}^s \\ \mathbf{f}_{pm}^g \end{Bmatrix}$.

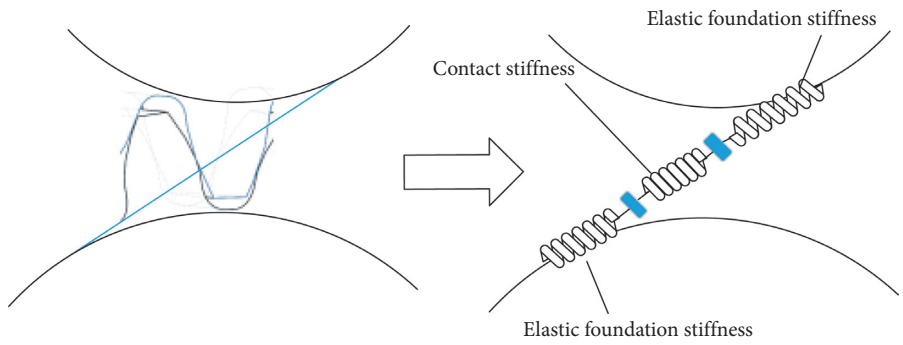

Figure 3: (a) Gear tooth meshing diagram. (b) Elastic foundation model for a pair of mating teeth.

The same method is used to the driven shaft (including gear and shaft). The mass matrix $\mathbf{M}_g$, stiffness matrix $\mathbf{K}_g$, and force vector $\mathbf{f}_g$ of the driven shaft can be obtained by the same way.

3. Mesh Stiffness Interface Modeling

In Section 2, the mass matrices, stiffness matrices, and force vectors of the driving and the driven shaft in the independent model coordinate were obtained. The relationship between them needs to be established by a pair of mating teeth. As shown in Figure 3, Bettaieb et al. [23, 25] used the Pasternak foundation to simulate the tooth contacts. In their model, a pair of mating teeth is assimilated to two different foundations (one for the pinion tooth and the other one for the gear tooth). The two foundations are linked in series by some independent springs which was used to simulate the contact stiffness (see in Figure 3). In this paper, assuming that the two foundations are located in the plane of action, the stiffness of Hertzian contact of two meshing teeth can be given by [26]

$$K_h = \frac{\pi EL}{4(1-\nu^2)}, \tag{10}$$

where E, L, and ν represent Young's modulus, tooth width and Poisson's ratio, respectively.

As shown in Figure 4, Pasternak's foundations are made of superposition of bending and shearing elements lying on independent springs. The differential equations of Pasternak's foundation can be written as follows [25]:

$$D(\eta)\frac{\partial^4 d(\eta)}{\partial^4 \eta} - G(\eta)\frac{\partial^2 d(\eta)}{\partial^2 \eta} + k(\eta)d(\eta) = P(\eta), \tag{11}$$

where $d(\eta)$ is the displacement at appoint of coordinate η; $P(\eta)$ is the applied force; and $D(\eta)$, $G(\eta)$, and $k(\eta)$ are the bending, shearing, and direct stiffness coefficients, respectively.

As shown in Figure 5, assuming that the tooth face has n contact lines, every contact line is represented by a foundation. Then, the instantaneous strain energy of the ith foundation discretized into N cells is

$$U_i = \frac{1}{2}\sum_{j=1}^{N}\left(k_{i,j}\left(d_{i,j}-\delta_{i,j}\right)^2\Delta\eta + G_{i,j}\left(\frac{\partial d_{i,j}}{\partial \eta}\right)^2\Delta\eta + D_{i,j}\left(\frac{\partial^2 d_{i,j}}{\partial^2 \eta}\right)^2\Delta\eta\right), \tag{12}$$

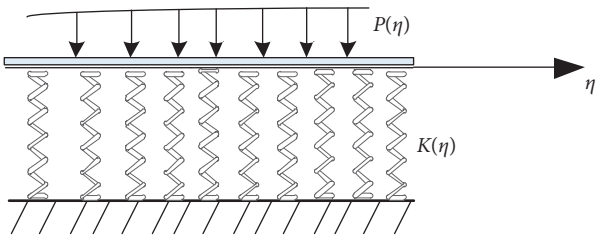

Figure 4: Pasternak's foundation model.

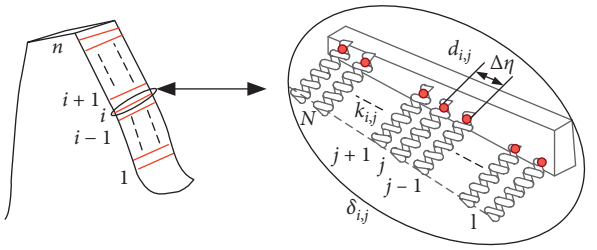

Figure 5: Tooth elastic foundation model.

where $k_{i,j}, G_{i,j}$, and $D_{i,j}$ are the direct, shearing, and bending stiffness coefficients per unit of the length at the jth cell of the ith foundation; $d_{i,j}$ is the displacement of the foundation; $\delta_{i,j}$ is the displacement of the gear body, which is corresponding to the kept DOFs $\mathbf{p}_k^g$ introduced in Section 2.1; $\Delta\eta$ is the length of a cell; and $k_{i,j}$ can be deduced by the potential method [11]. The determination of $G_{i,j}$ and $D_{i,j}$ can be consulted in reference [25].

The stiffness of the ith foundation can be obtained by using finite difference and Lagrange's equation.

4. Gear Dynamic Modeling

Figure 6 is the integrated model of a gear system. A parametrically excited dynamic equation can be obtained by assembling all the mass matrices, the stiffness matrices, and the force vectors:

$$\begin{bmatrix} 0 & 0 \\ 0 & \mathbf{M}_{qq} \end{bmatrix}\begin{bmatrix} \ddot{\mathbf{d}} \\ \ddot{\mathbf{q}} \end{bmatrix} + \begin{bmatrix} \mathbf{K}_{dd} & \mathbf{K}_{dq} \\ \mathbf{K}_{qd} & \mathbf{K}_{qq} \end{bmatrix}\begin{bmatrix} \mathbf{d} \\ \mathbf{q} \end{bmatrix} = \begin{bmatrix} \mathbf{f}_d \\ \mathbf{f}_q \end{bmatrix}, \tag{13}$$

where $\mathbf{d}$ is the displacement of elastic foundation; $\mathbf{M}_{qq}\mathbf{K}_{qq}$, and $\mathbf{q}$ are the mass matrix, stiffness matrix, and displacement

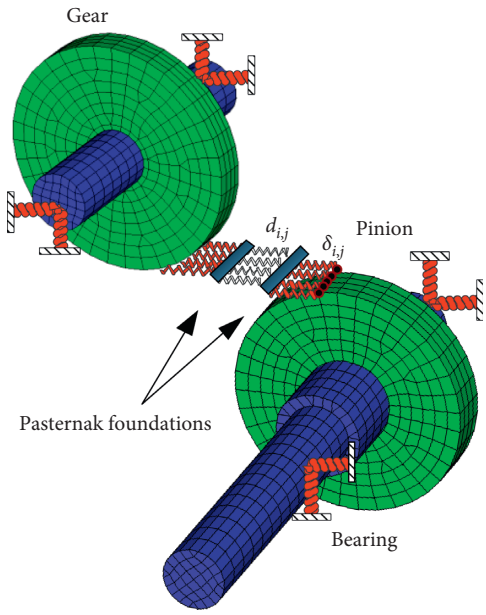

Figure 6: The 3D FEM of a gear system.

of the 3D FEM of the gear system, respectively; and $\mathbf{K}_{dd}$ is the stiffness of elastic foundation and $\mathbf{K}_{dq}$ is the coupling stiffness matrix of elastic foundation and 3D FEM of the gear system.

On the one hand, the mass matrix of equation (13) is a singular matrix. On the other hand, in order to reduce the number of DOF. The static condensation is needed for equation (13). According to equation (9), the foundation displacement vector $\mathbf{d}$ can be written as follows:

$$\mathbf{d} = \mathbf{K}_{dd}^{-1}\left(\mathbf{f}_d - \mathbf{K}_{dq}\mathbf{q}\right). \tag{14}$$

Then, equation (9) can be rewritten as follows:

$$\mathbf{M}_{qq}\ddot{\mathbf{q}} + \mathbf{C}_{t,q}\dot{\mathbf{q}} + \mathbf{K}_{t,q}\mathbf{q} = \mathbf{f}_{t,q}, \tag{15}$$

where $\mathbf{K}_{t,q} = \mathbf{K}_{qq} - \mathbf{K}_{qd}\mathbf{K}_{dd}^{-1}\mathbf{K}_{dq}$ and $\mathbf{f}_{t,q} = \mathbf{f}_q - \mathbf{K}_{qd}\mathbf{K}_{dd}^{-1}\mathbf{f}_{dq}$. The damping model is the Rayleigh damping, $\mathbf{C}_{t,q} = \beta\mathbf{K}_{t,q}$, where β is a damping coefficient and $\beta = 1 \times 10^{-7}$ in this paper.

4.1. The Model of Spalling. The references mentioned in the introduction mainly investigate the effect of gear tooth crack on vibration response. However, the spalling fault of gear is also a common failure type in engineering applications. The spalling fault usually happens near the pitch line of the gear. As shown in Figure 7(a), the spalling defect in this paper is modeled near the pitch line as a rectangular spalling. Figure 7(b) is the elastic foundation model corresponding to Figure 7(a). Assuming that the driving gear does not contact with the driven gear in the spalling area, the contact stiffness is removed in the spalling area. So, the contact stiffness in the spalling area can be obtained as follows:

$$K_h^s = \frac{\pi E\left(L - \Delta L\right)}{4\left(1 - \nu^2\right)}, \tag{16}$$

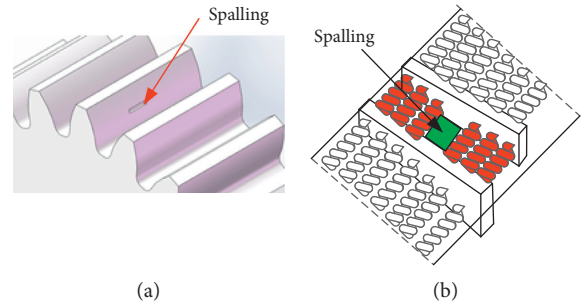

Figure 7: The model of spalling.

where ΔL is the reduction of the length of the contact line and other parameters have the same definition with equation (10).

5. Simulation and Experiment Results

The model validation is a very critical step. Therefore, the validity of the model was verified by static and dynamic analysis.

5.1. Static Behavior Analysis. As shown in Figure 8, the node forces were applied on the whole tooth face and the three middle nodes in the pitch circle, respectively. Constraints were imposed on the nodes shown in Figure 8(a). The same forces and constraints are applied to the proposed model. Figures 9(a) and 9(b) are the node displacement across the face width when the force was applied on the whole tooth face and on the three middle nodes, respectively. Compared with FEM, the maximum relative errors of node displacement of the two cases are 3.93% and 4.72%, respectively. It indicates that the deflection curves from the proposed method are in well agreement with those results obtained by 3D FEM.

5.2. Dynamic Behavior Analysis. In dynamic behavior analysis, two comparisons are used to verify the effectiveness of the proposed model. The first comparison is the comparison between the proposed method and experiments. The second comparison is the comparison between the proposed method and the hybrid beam element/lumped models.

5.2.1. The Comparison between the Proposed Method and Experiments. Simulation and experimental parameters are listed in Table 1. A photograph of a spur gear test rig is shown in Figure 10. Simulation results of dynamic responses are obtained by Newmark-β numerical integration. The comparison results between experimental signals and the simulation signals are shown in Figures 11 and 12. Figure 11(a) is the time-domain waveform of the simulation signal. It shows that the system will produce impact response, when the single and double teeth meshing, alternately. Each set of impact is composed of two alternating periodic shock responses with different amplitudes. The frequency of every two strong shocks or every two weak

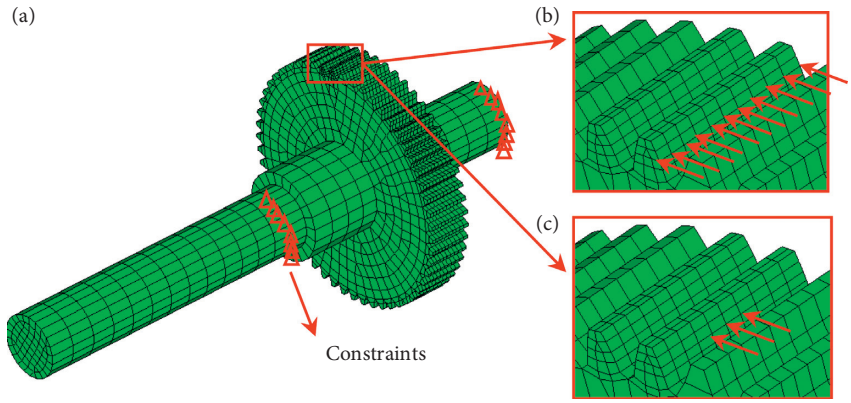

Figure 8: (a) The static model of the driving shaft and its constraints, (b) the node forces were applied on the whole tooth face, and (c) the node forces were applied on the three middle nodes in the pitch circle.

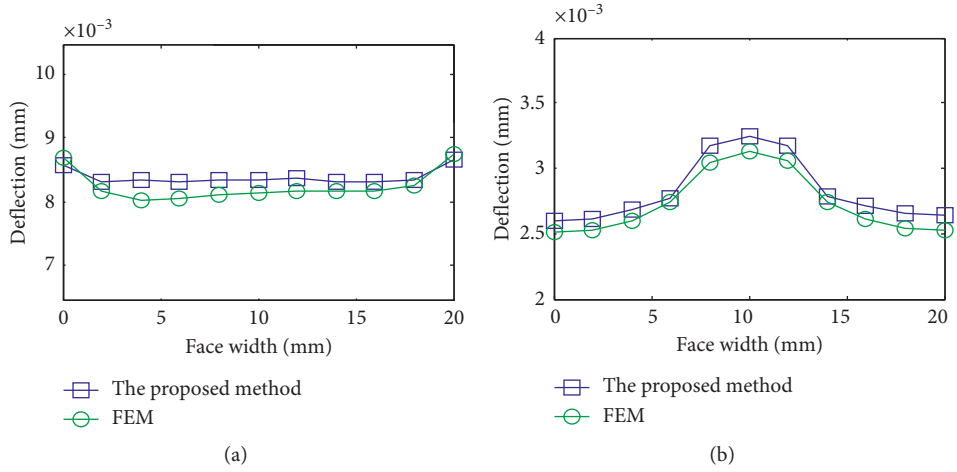

Figure 9: Deflection curve. The node force applied on the (a) whole tooth face ($f = 100$ N) and (b) middle of tooth face ($f = 70$ N).

Table 1: The parameters of spur gear rig.

	Driving gear	Driven gear
Number of teeth	55	75
Module (mm)	2	2
Pressure angle (°)	20	20
Young's modulus (Pa)	2.06×10^{11}	2.06×10^{11}
Poisson's ratio	0.3	0.3
Width of tooth (mm)	20	20
Rotational speed (Hz)	7.17	5.25
Torque (N·m)	6.8	5
Radial stiffness of bearing (N/m)	2×10^8	

shocks is 394 Hz (0.0025 s), which is equal to the meshing frequency of the gear system. In the experimental signal, this phenomenon is not very clear due to the background noise. The second generation wavelet transforms is used to process the original signal, and the forth sub-band is shown in Figure 11(b). It shows some of the same phenomena as the simulation signal. Figure 12 shows the spectrum of simulation signals and experimental signals. It can be found that the vibration signals of the normal gear are mainly the meshing frequency and its doubling frequency.

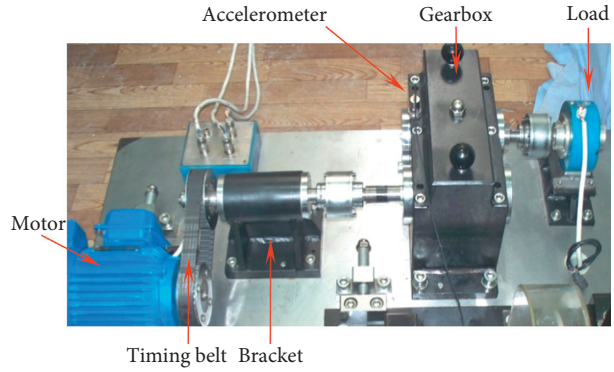

Figure 10: The spur gear test rig.

5.2.2. The Comparison Results between Hybrid Beam Element/Lumped Models and the Proposed Method. Based on the same parameters, the hybrid beam element/lumped models [11] and the proposed method were used to investigate the vibration characteristics, respectively. The comparison between them is shown in Figure 13. By comparison, it is found that the two models can show the impact response caused by the single and double teeth

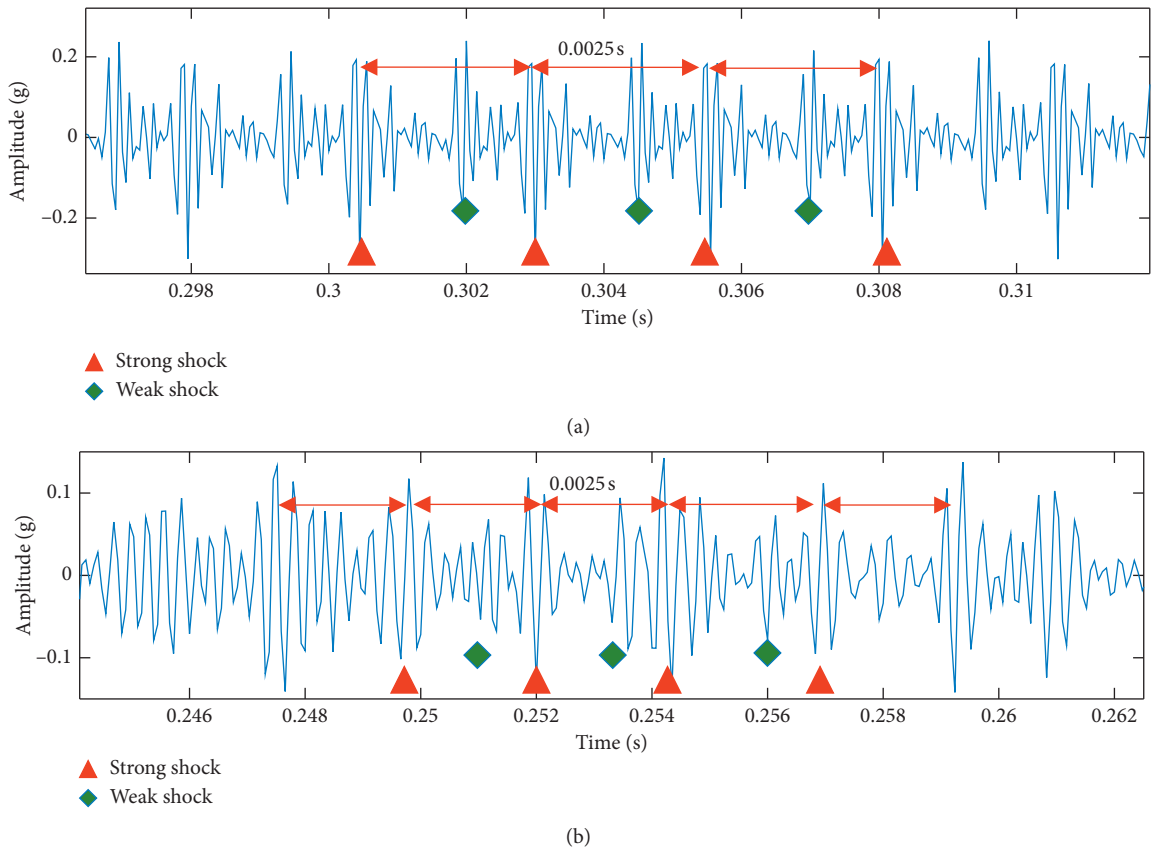

Figure 11: Time domain response of gear without defect. (a) The simulation signal. (b) The forth sub-band of experimental signal.

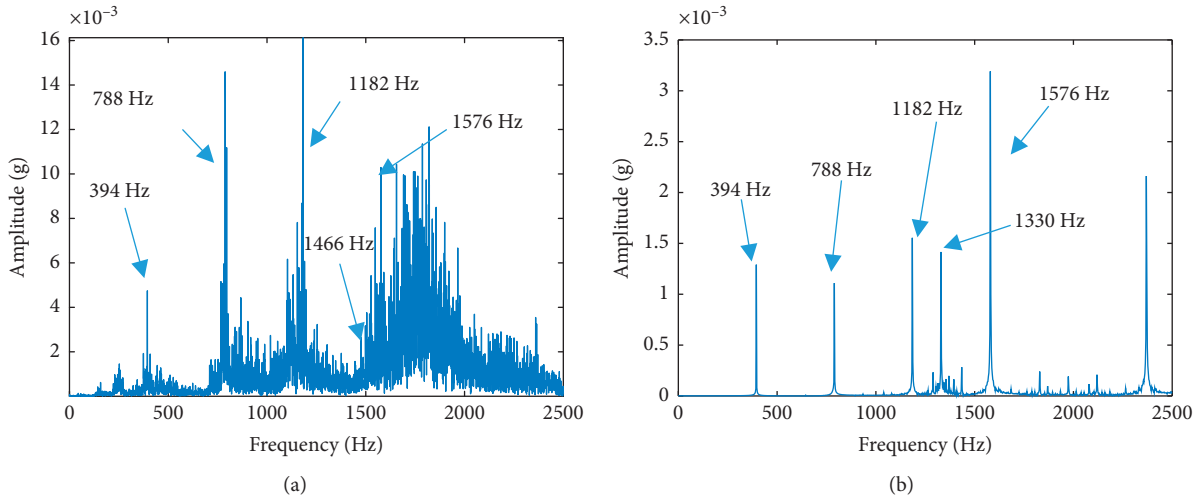

Figure 12: The spectrum of gear without defect. (a) The experimental signal and (b) the simulation signal.

meshing alternately. In addition, the computational efficiency of this model is similar to that of the hybrid beam element/lumped model. The solution time of 20,000 numerical points of the proposed model is 336 s and that of the hybrid beam element/lumped models model is about 220 s. This shows that the efficiency of the 3D dynamic model is solved. The validity of the model was also proved to some extent.

5.3. Spalling Fault Simulation. As shown in Figure 14, assuming that the gear with the spalling fault is located in the driving gear, the spalling area is 2 mm long and 1 mm wide, and other parameters are shown in Table 1. Figure 15(a) is the time-domain waveform of the simulation signal, and Figure 15(b) is the experimental signal. Both the simulation signals and experimental signals show that the spalling fault will cause shock response with significantly enhanced

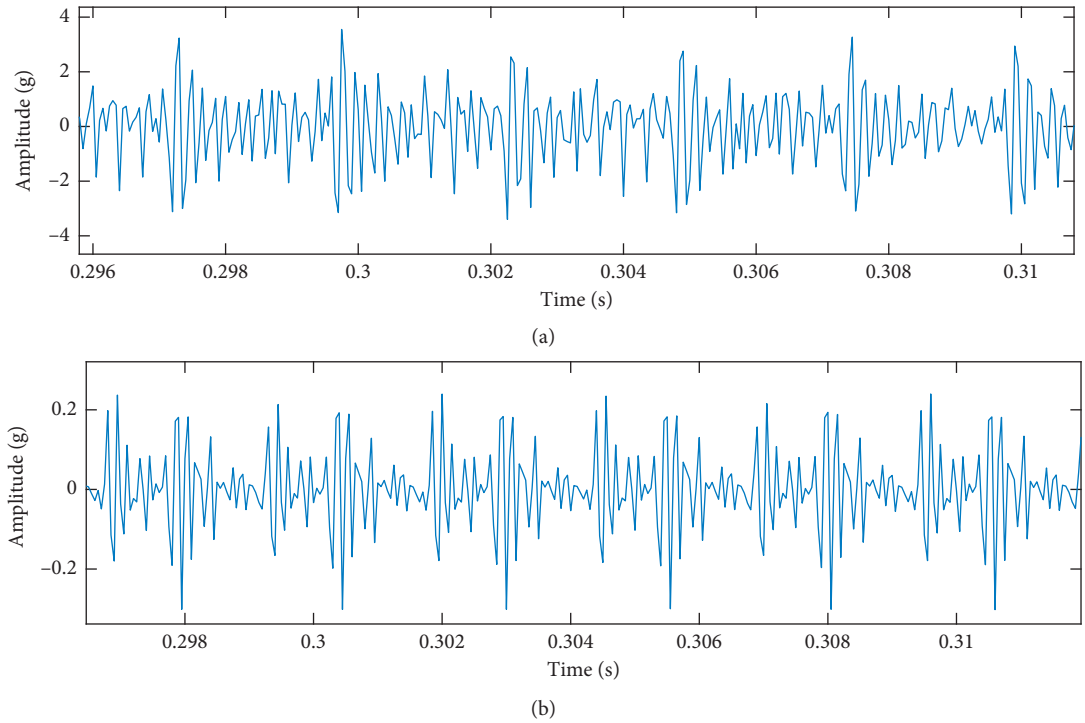

Figure 13: The simulation signal obtained by (a) the hybrid beam element/lumped models and (b) the proposed model.

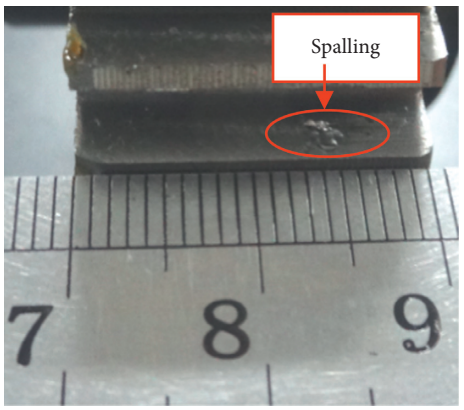

Figure 14: The spalling fault on the pinion.

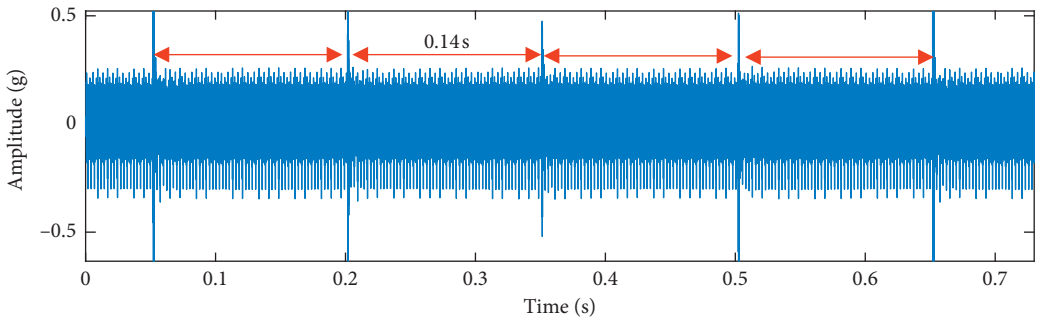

Figure 15: Continued.

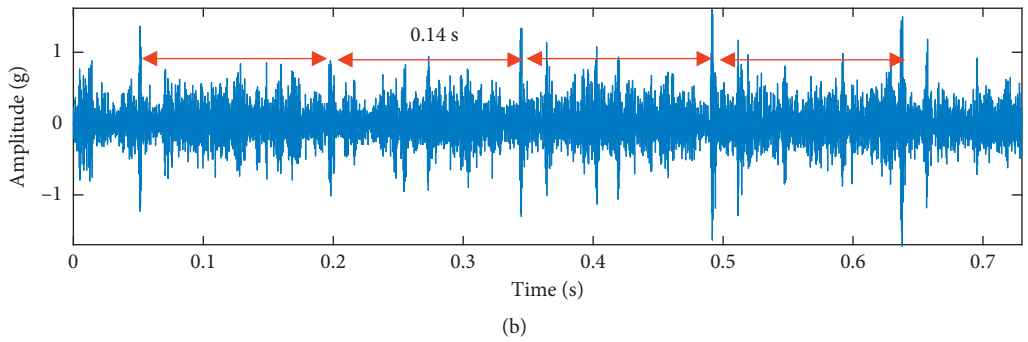

Figure 15: The time domain response waveform of gear with the spalling fault. (a) The simulation signal and (b) the experimental signal.

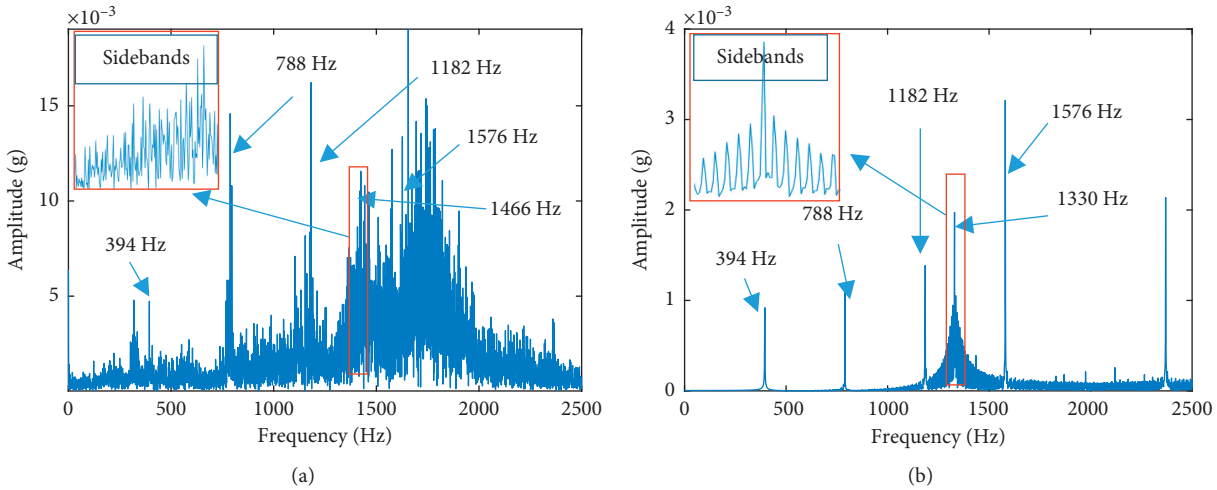

Figure 16: The spectrum of gear with spalling. (a) The experimental signal and (b) the simulation signal.

amplitude. The frequency of the shock response is equal to the rotation frequency of the driving shaft where the spalling gear is located. Figure 16 shows the spectrum of simulation signals and experimental signals of the gear with the spalling fault. By comparing Figures 12 and 16, it can be found that when the spalling fault occurs, the sidebands will appear in the spectrum. "Because of the short-period nature of the impact, the corresponding modulation sidebands will spread over a wide frequency range, which can produce high-order sidebands with low amplitudes. In the frequency domain, one can clearly observe sidebands with significant amplitudes starting in the resonance region (1446 Hz in Figure 16(a) and 1330 Hz in Figure 16(b)) and expand to higher frequencies [27]." These characteristics were successfully captured by the proposed dynamic model.

6. Conclusions

Dynamic modeling can improve the understanding of the diagnostic information that is buried in the vibration signal. A reduced-order dynamic model based on 3D FEM and CMS is proposed in this paper. In addition, the proposed model was used to study the effects of tooth spalling on dynamic vibration response. Based on the materials presented in this paper, conclusions can be summarized as below:

(1) The static analysis, dynamic analysis, and experimental analysis show that the proposed model is an effective model. The proposed model can be used to investigate the vibration characteristic of the spur gear system.

(2) The simulation results and experiment results show that the system will produce impact response, when the single and double teeth meshing, alternately. Each set of impact is composed of two alternating periodic shock responses with different amplitudes. The frequency of every two strong shocks or every two weak shocks is meshing frequency.

(3) The gear spalling fault will cause shock response with significantly enhanced amplitude. The frequency of the shock response is equal to the rotation frequency of the driving shaft where the spalling gear is located.

Future research should consider other influences on the vibration response, such as the friction, the inter-tooth backlash, the vibration of housing, and manufacturing errors in gears.

Data Availability

The data used to support the findings of this study are available from the corresponding author upon request.

Conflicts of Interest

The authors declare that they have no conflicts of interest.

Acknowledgments

This research was supported by the National Science and Technology Major Project (no. 2017ZX04011017), National Natural Science Foundation of China (NSFC) (no. 51674199), and Scientific Research Program funded by Shaanxi Provincial Education Department (Program no. 19JK0662).

References

[1] J. Xiang, Y. Lei, Y. Wang, Y. He, C. Zheng, and H. Gao, "Structural dynamical monitoring and fault diagnosis," *Shock and Vibration*, vol. 2015, Article ID 193831, 3 pages, 2015.

[2] R. Ma and Y. Chen, "Research on the dynamic mechanism of the gear system with local crack and spalling failure," *Engineering Failure Analysis*, vol. 26, pp. 12–20, 2012.

[3] Z. Chen and Y. Shao, "Dynamic simulation of spur gear with tooth root crack propagating along tooth width and crack depth," *Engineering Failure Analysis*, vol. 18, no. 8, pp. 2149–2164, 2011.

[4] C. H. Kang, W. C. Hsu, E. K. Lee, and T. N. Shiau, "Dynamic analysis of gear-rotor system with viscoelastic supports under residual shaft bow effect," *Mechanism and Machine Theory*, vol. 46, no. 3, pp. 264–275, 2011.

[5] W. Bartelmus, F. Chaari, R. Zimroz, and M. Haddar, "Modelling of gearbox dynamics under time-varying non-stationary load for distributed fault detection and diagnosis," *European Journal of Mechanics-A/Solids*, vol. 29, no. 4, pp. 637–646, 2010.

[6] Y. Xiong, K. Huang, F. Xu, Y. Yi, M. Sang, and H. Zhai, "Research on the influence of backlash on mesh stiffness and the nonlinear dynamics of spur gears," *Applied Sciences*, vol. 9, no. 5, p. 1029, 2019.

[7] J. Wang, G. He, J. Zhang, Y. Zhao, and Y. Yao, "Nonlinear dynamics analysis of the spur gear system for railway locomotive," *Mechanical Systems and Signal Processing*, vol. 85, pp. 41–55, 2017.

[8] W. Yang, D. Jiang, and T. Han, "Effects of tooth breakage size and rotational speed on the vibration response of a planetary gearbox," *Applied Science*, vol. 7, no. 7, p. 678, 2017.

[9] A. S. Mohamed, S. Sassi, and M. R. Paurobally, "Model-based analysis of spur gears' dynamic behavior in the presence of multiple cracks," *Shock and Vibration*, vol. 2018, Article ID 1913289, 20 pages, 2018.

[10] Z. Chen, W. Zhai, Y. Shao, K. Wang, and G. Sun, "Analytical model for mesh stiffness calculation of spur gear pair with non-uniformly distributed tooth root crack," *Engineering Failure Analysis*, vol. 66, pp. 502–514, 2016.

[11] Z. Wan, H. Cao, Y. Zi, W. He, and Z. He, "An improved time-varying mesh stiffness algorithm and dynamic modeling of gear-rotor system with tooth root crack," *Engineering Failure Analysis*, vol. 42, pp. 157–177, 2014.

[12] Q. Han, J. Zhao, W. Lu, Z. Peng, and F. Chu, "Steady-state response of a geared rotor system with slant cracked shaft and time-varying mesh stiffness," *Communications in Nonlinear Science and Numerical Simulation*, vol. 19, no. 4, pp. 1156–1174, 2014.

[13] Q. Han, J. Zhao, and F. Chu, "Dynamic analysis of a geared rotor system considering a slant crack on the shaft," *Journal of Sound and Vibration*, vol. 331, no. 26, pp. 5803–5823, 2012.

[14] H. Ma, X. Pang, R. Feng, R. Song, and B. Wen, "Fault features analysis of cracked gear considering the effects of the extended tooth contact," *Engineering Failure Analysis*, vol. 48, pp. 105–120, 2015.

[15] H. Ma, R. Song, X. Pang, and B. Wen, "Fault feature analysis of a cracked gear coupled rotor system," *Mathematical Problems in Engineering*, vol. 2014, Article ID 832192, 22 pages, 2014.

[16] W. Yu, C. K. Mechefske, and M. Timusk, "The dynamic coupling behaviour of a cylindrical geared rotor system subjected to gear eccentricities," *Mechanism and Machine Theory*, vol. 107, pp. 105–122, 2017.

[17] H. Ma, J. Zeng, R. Feng, X. Pang, Q. Wang, and B. Wen, "Review on dynamics of cracked gear systems," *Engineering Failure Analysis*, vol. 55, pp. 224–245, 2015.

[18] X. Liang, M. J. Zuo, and Z. Feng, "Dynamic modeling of gearbox faults: a review," *Mechanical Systems and Signal Processing*, vol. 98, pp. 852–876, 2018.

[19] S. Liu, C. Song, C. Zhu, C. Liang, and X. Yang, "Investigation on the influence of work holding equipment errors on contact characteristics of face-hobbed hypoid gear," *Mechanism and Machine Theory*, vol. 138, pp. 95–111, 2019.

[20] G. Meneghetti, C. Guzzella, and B. Atzori, "The peak stress method combined with 3d finite element models for fatigue assessment of toe and root cracking in steel welded joints subjected to axial or bending loading," *Fatigue & Fracture of Engineering Materials & Structures*, vol. 37, no. 7, pp. 722–739, 2018.

[21] P. Lopez-Crespo, D. Camas, F. V. Antunes, and J. R. Yates, "A study of the evolution of crack tip plasticity along a crack front," *Theoretical and Applied Fracture Mechanics*, vol. 98, pp. 59–66, 2018.

[22] A. D. Spear, J. D. Hochhalter, A. R. Cerrone et al., "A method to generate conformal finite-element meshes from 3d measurements of microstructurally small fatigue-crack propagation," *Fatigue & Fracture of Engineering Materials & Structures*, vol. 39, no. 6, pp. 737–751, 2016.

[23] M. N. Bettaïeb, P. Velex, and M. Ajmi, "A static and dynamic model of geared transmissions by combining substructures and elastic foundations-applications to thin-rimmed gears," *Journal of Mechanical Design*, vol. 129, no. 2, pp. 184–194, 2007.

[24] T. Lin, H. Ou, and R. Li, "A finite element method for 3d static and dynamic contact/impact analysis of gear drives," *Computer Methods in Applied Mechanics and Engineering*, vol. 196, no. 9–12, pp. 1716–1728, 2007.

[25] M. Ajmi and P. Velex, "A model for simulating the quasi-static and dynamic behaviour of solid wide-faced spur and helical gears," *Mechanism and Machine Theory*, vol. 40, no. 2, pp. 173–190, 2005.

[26] P. Sainsot, P. Velex, and O. Duverger, "Contribution of gear body to tooth deflections—a new bidimensional analytical formula," *Journal of Mechanical Design*, vol. 126, no. 4, pp. 748–752, 2004.

[27] Y. Luo, N. Baddour, and M. Liang, "Dynamical modeling and experimental validation for tooth pitting and spalling in spur gears," *Mechanical Systems and Signal Processing*, vol. 119, pp. 155–181, 2019.